# Doubly differential detachment cross sections for 0.5-MeV $H^-$ on He including projectile excitation to $H(n=2)$

Chih-Ray Liu and Anthony F. Starace
*Department of Physics and Astronomy, The University of Nebraska, Lincoln, Nebraska 68588-0111*
(Received 30 May 1989; revised manuscript received 21 July 1989)

Detailed theoretical results are presented for the electron-detachment cross section, doubly differential in both the electron momentum and angle, for the process 0.5-MeV $H^- + He \rightarrow H(n=2) + e^- + He^*$. As discussed briefly elsewhere [C. R. Liu and A. F. Starace, Phys. Rev. Lett. **62**, 407 (1989)], the laboratory-frame doubly differential cross sections (DDCS's) for electron detachment in the forward direction are shown to depend sensitively on the low-energy states of the $H(n=2)$-$e^-$ three-body system. In particular, the angular dependence of characteristic cusp and shape resonance features is presented. We find that the projectile frame DDCS for detached electron energies in the vicinity of the shape resonance peak is nearly isotropic. This is due in part to the $^1P$ symmetry of the resonance feature, which limits the angular distribution to constant and $\cos^2\theta$ terms, and in part to cancellation in the integral over momentum transfer on which the coefficient of the $\cos^2\theta$ term depends. We also find that the rapid variation of these cusp and shape resonance features with angle in the laboratory frame requires that experimental angular and energy resolutions be accounted for in order to obtain good agreement with the measured results of M. G. Menendez and M. M. Duncan [Phys. Rev. A **36**, 1653 (1987)] on the energy spectrum of detached electrons coincident with the formation of $H(2p)$. The DDCS's for 0.5-MeV $H^- + He \rightarrow H(1s) + e^- + He^*$ are also presented. When these latter results are added to those for producing $H(n=2)$, the sum gives good agreement with the experimental data of M. G. Menendez and M. M. Duncan [Phys. Rev. **20**, 2327 (1979)], which include all final states of the H atom, thereby confirming the important contribution the $H(n=2)$ states make to the total-detachment cross section. We present evidence on the sensitivity of these results to the choice of the average excitation energy of the helium target. Finally, we pinpoint the origin of our predicted Gailitis-Damburg oscillations in the DDCS near threshold as stemming from a rapid decrease of an analytically known phase appropriate for long-range dipole fields.

## I. INTRODUCTION

The cross section for high-energy $H^-$ detachment collisions, particularly that differential in the energy and angle of the detached electron, depends sensitively on the low-energy states of the fundamental H-$e^-$ three-body system. These low-energy states in the $H^-$ frame are related kinematically to the small-angle (i.e., forward-direction) behavior of the detachment cross section measured in the laboratory. These same kinematic relations, furthermore, magnify the energy scale over which the fundamental dynamics of the H-$e^-$ system may be observed: e.g., for the 0.5-MeV $H^-$ detachment collisions studied here, features in the $H^-$ frame measured on a scale of tens of meV appear in the laboratory frame on a scale of tens of eV. The prime requisite for any theory of such fast $H^-$ detachment collisions therefore is a reasonable dynamical description of the low-energy states of the H-$e^-$ three-body system.

We present here such a theoretical description for the following detachment collision process:

$$0.5\text{-MeV } H^- + He \rightarrow H(n=2) + e^- + He^* \ . \quad (1)$$

The asterisk on the right-hand side of Eq. (1) indicates that the He atom may be either in an excited state, bound or continuum or in the unexcited ground state. This process is particularly interesting because, first, the degeneracy of the $H(2s)$ and $H(2p)$ energy levels leads to an attractive long-range dipole potential acting on the detached electron.[1,2] Second, one of the $^1P^\circ$ channels of the $H(n=2)$-$e^-$ system has a well-known shape resonance approximately 18 meV above the detachment threshold.[3] We have already discussed briefly elsewhere[4] how these dynamical features of the $H(n=2)$-$e^-$ system affect the laboratory-frame doubly differential cross section (DDCS) in the forward direction. Here we present a more complete discussion, emphasizing in particular the angular dependence of the laboratory-frame DDCS.

Although the subject of negative-ion detachment collisions has a long history, the number of experimental and other theoretical works relevant to the present calculations is rather limited. Collisional detachment of negative ions was the subject of a symposium at the International Conference on the Physics of Electronic and Atomic Collisions (ICPEAC) in Kyoto in 1979.[5] In particular, Risley[6] presented a comprehensive tabulation of all such processes which had been studied experimentally and theoretically to mid-1979. More recent reviews are also available.[7,8] Nearly all of this work up to the early 1980s, however, has been devoted to *total* detachment cross sections despite the fact that electron DDCS's are

 

known to provide much more detailed information on ion-atom collision dynamics than do total cross sections for electron production.[9,10]

A notable exception since the late 1970s has been the work of Menendez, Duncan, and co-workers,[11] who have studied experimentally the doubly differential collisional electron detachment cross section of $H^-$ by He and related processes, primarily at an incident ion energy of 0.5 MeV. Initially, they measured the energy distribution of the detached electrons at several fixed laboratory angles for the following process:[11(b)-11(d)]

$$H^- + He \rightarrow H^* + He^* + e^- \ . \tag{2}$$

These experiments did not distinguish among the various possible final states of excitation of the heavy particles. A key feature of the experimental data is that for electrons detached at angles close to 0° in the laboratory frame, the intensity distribution of electrons, as a function of electron kinetic energy, has two peaks, separated by about 30 eV, instead of the more usual single peak predicted by the binary encounter theory.[10] The observed higher-energy peak, which occurs at an electron velocity equal to the incident $H^-$ velocity, decreases in intensity with increasing laboratory-frame scattering angle, and it disappears altogether for angles greater than about 4°.

This experimental work led to a number of theoretical studies[12-16] for the dominant process in Eq. (2), i.e.,

$$H^- + He \rightarrow H(1s) + He^* + e^- \ , \tag{3}$$

in which the hydrogen atom is not excited during the collision. Qualitatively, the main features of the experimental data were understood theoretically. In particular, the double-peak structure seen experimentally was shown to arise theoretically from an interference of $s$ and $p$ partial waves for the detached electron.[12,14,16] This interference is most visible in the projectile-frame doubly differential cross section.[14,16] Furthermore, this interference is more significant the larger the mean excitation energy of the target atom or molecule,[11(c)] thereby explaining why it is particularly apparent for He targets.

Quantitative agreement between the experimental results[11(b)-11(d)] for process (2) and even the most detailed calculation[16] for process (3), while very good for laboratory angles greater than 4°, is poor for smaller laboratory angles. Specifically, while for small angles the predicted lower-energy peak agrees reasonably with the experimental results, the predicted higher-energy peak occurs higher in energy and is lower in magnitude than observed experimentally. Since the theoretical calculations restricted the H atom to the 1$s$ level, they offered indirect proof of the importance of H-atom excitation states to the observed-higher energy peak. This conclusion is also supported by more direct evidence: the calculations of Wright *et al.*,[17] which include excitation of H to the 2$s$ level, and the more recent experimental results of both Duncan, Menendez, and co-workers[11(f)-11(h)] and of Andersen, Sørensen, and co-workers,[18] both of which include specific forward-angle measurements of collisional excitation of the $n=2$ states of H.[11(g),11(h),18(a)]

A major result of the calculations reported here is substantially improved quantitative agreement with the experimental results for process (2), in which the final state of H is not measured, when we add our calculated cross sections for $H(n=2)$ [process (1)] to our calculated cross sections for $H(1s)$ [process (3)]. Thus we confirm that projectile detachment plus excitation is a major contributor to the equal-velocity peak in the detached-electron DDCS's seen experimentally at and near 0° in the laboratory. Furthermore, our calculated cross sections for $H(n=2)$ [process (1)] agree with experimental findings that near 0° in the laboratory, the electron angular distribution of the equal-velocity peak is isotropic in the projectile frame.[11(f)] This isotropy may be understood in our calculations as due to the dominance of the $^1P^o$ shape-resonance channel of the $H(n=2)$-$e^-$ system and to a cancellation in the momentum-transfer integral for the coefficient of the $\cos^2\theta$ term of the projectile-frame DDCS, as we discuss below. In addition, our calculated DDCS's for electron detachment with excitation of $H(2p)$ are in excellent agreement with experiment[11(g)] when we take proper account of the experimental energy and angular resolutions. Finally as discussed briefly elsewhere[4] and as presented in more detail here, our prediction of cusp, shape resonance, and Gailitis-Damburg[2] oscillation features in the DDCS's for process (1) at small electron-detachment angles are all effects of the low-energy dynamics of the $H(n=2)$-$e^-$ three-body system. These effects are just beginning to be observed experimentally.[11(h),18(a)]

In Sec. II we present the key approximations employed in carring out our calculations. In Sec. III we present our results for both processes (1) and (3). Finally, in Sec. IV we discuss our results and present our conclusions. In the Appendix, we present some relevant details concerning the analytic extraction of dipole-field-induced oscillations of the transition matrix elements.

## II. THEORETICAL FORMULATION FOR THE DOUBLY DIFFERENTIAL DETACHMENT CROSS SECTION

A detailed theoretical presentation of the DDCS for process (3), in which the H atom is left in the 1$s$ level in the final state, has been given by Park *et al.*[16,19] Our interest here is in process (1), in which the H atom is excited to the 2$s$ or the 2$p$ level in the final state. This different focus, however, only affects the calculation of the $H^-$ projectile transition form factor. In the interest of brevity, therefore, we shall concern ourselves in this section with those aspects of the theoretical formulation that are specific to the calculation of the DDCS for process (1) and shall otherwise refer the reader to Ref. 16 (and references therein).[19]

### A. First Born expression for the DDCS in the closure approximation

The Born approximation result for the DDCS for electron detachment following collision of the projectile-ion $H^-$ with the target atom He may be expressed in terms of the atomic form factor $[\epsilon_{00}^{He}(K)]$ and incoherent scattering function $[S_{inc}^{He}(K)]$ for helium as[20]

$$\frac{d\sigma}{d\omega\, dE}=k\Sigma^G_{nl}(k_P,\theta_P)\ , \tag{4a}$$

where

$$\Sigma^G_{nl}(k_P,\theta_P)=\frac{8\pi}{v_i^2}\int_{K_{\min}(0)}^{K_{\max}(0)} J_{nl}(K,k_P,\theta_P)|\epsilon^{\rm He}_{00}(K)-2|^2\frac{dK}{K^3}$$
$$+\frac{8\pi}{v_i^2}\int_{K_{\min}(\bar I_{\rm He})}^{K_{\max}(\bar I_{\rm He})} J_{nl}(K,k_P,\theta_P)S^{\rm He}_{\rm inc}(K)\frac{dK}{K^3}\ . \tag{4b}$$

In Eq. (4a), $k$ is the momentum, $d\omega$ is the solid angle, and $E$ is the energy of the detached electron in any convenient inertial reference frame. $\Sigma^G_{nl}(k_P,\theta_P)$ is a Galilean invariant cross section[14] calculated in the center-of-mass frame and is dependent on the detached-electron's momentum $k_P$ relative to the H atom as well as on the angle $\theta_P$ that $\mathbf{k}_P$ makes with the axis defined by the incident projectile ($P$); $nl$ denotes the final state of the H atom. $\Sigma^G_{nl}(k_P,\theta_P)$ is defined by Eq. (4b), where $v_i$ is the relative velocity of the projectile with respect to the target ($v_i=4.471\,35$ a.u. for 0.5-MeV $H^-$ incident on He); $\mathbf{K}$ is the momentum transfer,

$$\mathbf{K}\equiv\mathbf{k}_i-\mathbf{k}_f\ , \tag{5}$$

where $\mathbf{k}_i$ and $\mathbf{k}_f$ are the initial and final momenta of the projectile in the center-of-mass frame; $K_{\min}(0)$ and $K_{\max}(0)$ are the appropriate minimum and maximum values for the momentum transfer for the case in which the He target remains unexcited, while $\bar I_{\rm He}$ in $K_{\min}(\bar I_{\rm He})$ and $K_{\max}(\bar I_{\rm He})$ implies that these latter are computed for some appropriate average excitation energy $\bar I_{\rm He}$ for the target. The use of $\bar I_{\rm He}$ and the closure approximation substitutes for an explicit summation over each of the excited states of the target.[21] Explicit values for the atomic form factor and the incoherent scattering function for helium have been given by a number of authors.[22–24] We have employed in our calculations those of Hubbell *et al.*[23] Finally, the function $J_{nl}(K,k_P,\theta_P)$ is defined by

$$J_{nl}(K,k_P,\theta_P)=\frac{1}{2\pi}\int_0^{2\pi}\sum_m|\epsilon^{H^-}_{nlm}(\mathbf{K},\mathbf{k}_P)|^2 d\phi\ . \tag{6}$$

In Eq. (6) the transition form factor is defined by

$$\epsilon^{H^-}_{nlm}(\mathbf{K},\mathbf{k}_P)\equiv\left\langle\psi^-_{nlm\mathbf{k}_P}\left|\sum_{i=1}^{2}\exp(i\mathbf{K}\cdot\mathbf{r}_i)\right|\psi_0\right\rangle \tag{7}$$

and corresponds to a transition from the ground state of $H^-$ to the final state of the H-$e^-$ system in which the electron is detached with momentum $\mathbf{k}_P$ relative to the H atom and the H atom is left in the state H($nlm$). The ground state of $H^-$ is described by the wave function $\psi_0$ and the final state of the H-$e^-$ system is described by the wave function $\psi^-_{nlm\mathbf{k}_P}$, where the minus superscript indicates that it satisfies incoming-wave boundary conditions. Equation (6) contains a summation over the magnetic sublevels of the H($nlm$) state as well as an integration over the azimuthal angle $\phi$ of the scattered projectile in the center-of-mass frame. This latter integration makes $J_{nl}$ independent of the azimuthal angle $\phi_P$ of the detached electron.

### B. Reference frames

The DDCS in any convenient inertial reference frame is expressed in Eq. (4a) in terms of the Galilean invariant DDCS $\Sigma^G_{nl}(k_P,\theta_P)$, which is calculated according to Eq. (4b) in the center-of-mass frame. In particular, the laboratory ($L$) frame DDCS is given by

$$\left[\frac{d\sigma}{d\omega\, dE}\right]_L=k_L\Sigma^G_{nl}(k_P(k_L,\theta_L),\theta_P(k_L,\theta_L))\tag{8}$$

where $k_L$ and $\theta_L$ are the magnitude and polar angle of the detached-electron's momentum in the laboratory and where $k_P$ and $\theta_P$ are expressed as functions of $k_L$ and $\theta_L$. In general, the functional dependence of $k_P$ and $\theta_P$ on $k_L$ and $\theta_L$ is complicated since the projectile in any scattering process is deflected from its incident direction. In other words, the reference frame sited on the projectile is, in general, *not* an inertial reference frame. To a good approximation, however, for the fast $H^-$ detachment collisions considered here, it is known that nearly all the momentum transfer is absorbed by the detached electron rather than by the H atom.[10,14] Hence, the so-called projectile reference frame[10,14] is approximately an inertial reference frame.

This approximation simplifies the relation between $\mathbf{k}_L$ and $\mathbf{k}_P$ to

$$\mathbf{k}_L=\mathbf{v}_i+\mathbf{k}_P\ . \tag{9}$$

Furthermore, we may then define a projectile ($P$) frame DDCS as[10,14]

$$\left[\frac{d\sigma}{d\omega\, dE}\right]_P=k_P\Sigma^G_{nl}(k_P,\theta_P)\ . \tag{10}$$

The low-energy dynamics of the H-$e^-$ system is clearly exhibited in the projectile-frame DDCS in Eq. (10) and the simple relation (9) facilitates the subsequent interpretation of the laboratory-frame DDCS in Eq. (8).

### C. $H^-$ wave functions

#### 1. *General boundary and normalization conditions*

In order to calculate the $H^-$ transition form factor in Eq. (7), we require the incoming-wave normalized wave function describing a final state in which asymptotically the H atom is excited to its $nlm$ level and the detached electron is departing with relative momentum $\mathbf{k}_P$. That is, we wish this wave function to satisfy the boundary condition

$$\psi^-_{nlm\mathbf{k}_P}(\mathbf{r}_1,\mathbf{r}_2)\underset{r_1\to\infty}{\sim}(2\pi)^{-3/2}r_2^{-1}P_{nl}(r_2)Y_{lm}(\hat{\mathbf{r}}_2)$$
$$\times\exp(i\mathbf{k}_P\cdot\mathbf{r}_1)+\cdots \tag{11}$$

where the ellipsis represents incoming spherical waves, and, to be normalized to a $\delta$ function in momentum,

$$\int d^3\mathbf{r}_1 \int d^3\mathbf{r}_2 (\psi^-_{n'l'm'\mathbf{k}'_P})^\dagger \psi^-_{nlmk_P} = \delta_{nn'}\delta_{ll'}\delta_{mm'}\delta(\mathbf{k}_P-\mathbf{k}'_P) \ . \quad (12)$$

As usual, it is convenient theoretically to express this wave function in terms of a spherical wave expansion

$$\psi^-_{nlm\mathbf{k}_P}(\mathbf{r}_1,\mathbf{r}_2) = k_P^{-1/2} \sum_{l'm'} \sum_{LM} \psi^-_{ll'k_PLM}(\mathbf{r}_1,\mathbf{r}_2) i^{l'} \times \langle LM|lml'm'\rangle Y^*_{l'm'}(\hat{\mathbf{k}}_P) \ . \quad (13)$$

In Eq. (13), $\psi^-_{ll'k_PLM}(\mathbf{r}_1,\mathbf{r}_2)$ is the wave function appropriate for a final state comprising the H atom in the $nl$ level plus the detached electron having energy $\frac{1}{2}k_P^2$ and having an angular momentum $l'$. The orbital angular momenta of the detached electron and the H atom are coupled to form the total orbital angular momentum $L$ with azimuthal quantum number $M$. We ignore spin; $S=0$ always. Also, the spherical harmonic $Y^*_{l'm'}(\hat{\mathbf{k}}_P)$ projects the state $l'm'$ onto the direction $\mathbf{k}_P$, $\langle LM|lml'm'\rangle$ is a Clebsch-Gordan coefficient, $i^{l'}$ is a phase factor needed for the incoming-wave boundary condition, and $k_P^{-1/2}$ is needed to ensure the momentum normalization in Eq. (12).

Ordinarily the calculation of $\psi^-_{ll'k_PLM}$ from the two-electron Schrödinger equation is straightforward. A complication for the case of interest here is that the $2s$ and $2p$ levels of the H atom are degenerate. This degeneracy leads to a long-range dipole interaction between the H($n=2$) states and the detached electron.[1] This long-range interaction is not diagonal in the individual angular momenta $l$ and $l'$ of the H atom and the detached electron. Rather it is diagonal in the so-called dipole representation,[1,2,3(a)] which is why we choose a basis of functions which reduces asymptotically to the dipole representation.

### 2. *Adiabatic hyperspherical representation*

In our calculations we describe the H($n=2$)-$e^-$ three-body system in an adiabatic hyperspherical representation[25–27] since this is known to describe fairly accurately the key dynamical features of this system[4,28] and since this representation is known to diagonalize asymptotically the long-range dipole interaction for this system.[25,28] Accordingly, the wave functions $\psi^-_{ll'k_PLM}$ are expanded in a complete set of adiabatic eigenfunctions dependent on a hyperradius $R\equiv(r_1^2+r_2^2)^{1/2}$ and the five angular variables $\alpha\equiv\tan^{-1}(r_2/r_1)$, $\hat{\mathbf{r}}_1$, and $\hat{\mathbf{r}}_2$,

$$\psi^-_{ll'k_PLM}(\mathbf{r}_1,\mathbf{r}_2) = \sum_\mu \psi^-_{\mu k_P}(R,\alpha,\hat{\mathbf{r}}_1,\hat{\mathbf{r}}_2) \times e^{-i\xi_\mu} A^\dagger_{\mu,(ll')} e^{-i(1/2)\pi l'} \ , \quad (14a)$$

where the hyperspherical function for the $\mu$th channel is

$$\psi^-_{\mu k_P}(R,\alpha,\hat{\mathbf{r}}_1,\hat{\mathbf{r}}_2) \equiv (R^{5/2}\cos\alpha\sin\alpha)^{-1} \times \phi_\mu(R,\alpha,\hat{\mathbf{r}}_1,\hat{\mathbf{r}}_2) F_{\mu k_P}(R) e^{-i\eta_\mu} \ . \quad (14b)$$

In Eq. (14b), the prefactor on the right-hand side is a weight factor;[25] $\phi_\mu$ is the adiabatic hyperspherical angle function, which is a function of the five angles $\alpha$, $\hat{\mathbf{r}}_1$, and $\hat{\mathbf{r}}_2$ and is dependent only parametrically on $R$; $F_{\mu k_P}(R)$ is an energy-normalized radial function of $R$ for the $\mu$th channel and $\eta_\mu$ is its phase shift, which is defined later below. In Eq. (14a), $\xi_\mu$ is an analytically known phase, also defined later below, which characterizes the asymptotic behavior of the radial function $F_{\mu k_P}(R)$, and $\mathbf{A}$ is the matrix which diagonalizes the long-range dipole interaction in the basis of angular-momentum pairs $(ll')$.

The adiabatic hyperspherical approximation is described in detail elsewhere.[25–27] Furthermore, it has been reviewed for the calculations for process (3) in Ref. 16. For our present purposes we therefore only summarize its key features here and refer the reader to these other references for further details. The angle functions $\phi_\mu$ satisfy an angular equation[25–27] having eigenvalue $U_\mu(R)$. Here $\mu$ labels a particular solution of this angular equation for specified values of total orbital and spin angular momentum. [We have suppressed the specification of these total angular-momentum quantum numbers on the right-hand side of Eq. (14a) for simplicity of notation.] The radial functions $F_{\mu k_P}(R)$ satisfy a set of coupled radial equations;[25–27] however, in the adiabatic approximation[25] all but the diagonal coupling matrix elements are dropped so that each $F_{\mu k_P}(R)$ satisfies a one-dimensional radial Schrödinger equation

$$\left[\frac{d^2}{dR^2} - V_\mu(R) + k^2\right] F_{\mu k}(R) = 0 \ . \quad (15)$$

In Eq. (15) the effective radial potential $V_\mu(R)$, which characterizes the dynamical features of a particular hyperspherical channel $\mu$ converging to the $n$th level of the H atom, is defined by

$$-V_\mu(R) \equiv \frac{U_\mu(R)+\frac{1}{4}}{R^2} + \left\langle \phi_\mu, \frac{d^2\phi_\mu}{dR^2} \right\rangle + \frac{1}{n^2} \ , \quad (16)$$

where $\langle \phi_\mu, d^2\phi_\mu/dR^2\rangle$ is the $R$-dependent diagonal coupling matrix element for the $\mu$th channel. Since the long-range dipole interaction due to the degeneracy of the H($n=2$) states[1] is diagonal in the hyperspherical representation,[25,28] the asymptotic form of the effective radial potential is

$$V_\mu(R) \underset{R\to\infty}{\sim} \lambda_\mu(\lambda_\mu+1)/R^2 \ . \quad (17)$$

Here $\lambda_\mu$ is an effective orbital angular momentum, which may be real or complex depending on the channel $\mu$. Finally in Eq. (14a), the matrix $A$ with elements $A_{\mu,(ll')}$ transforms the dipole interaction eigenstate channels $\mu$ to the basis $(ll')$.

### 3. *Asymptotic forms*

We give here the asymptotic forms of the adiabatic hyperspherical angle and radial functions, since these are needed to verify the boundary condition in Eq. (11) for the total wave function. The energy-normalized radial wave functions satisfying the incoming-wave boundary

condition tend asymptotically to

$$F_{\mu k}(R) \underset{R\to\infty}{\sim} (2/\pi k)^{1/2}\sin(kR+\xi_\mu+\eta_\mu) , \tag{18}$$

where $\eta_\mu$ is the phase shift in the $\mu$th channel and $\xi_\mu$ is an analytic phase dependent on the effective angular momentum $\lambda_\mu$ characterizing the long-range dipole interaction of the H($n=2$)-$e^-$ system.[29] *For real values of* $\lambda_\mu$,

$$\xi_\mu \equiv -\tfrac{1}{2}\pi\lambda_\mu , \tag{19a}$$

while *for complex values of* $\lambda_\mu$, one may write, quite generally,[29]

$$\lambda_\mu = -\tfrac{1}{2}+i\alpha_\mu , \tag{19b}$$

in which case[29]

$$\xi_\mu \equiv -\tfrac{1}{4}\pi+\theta_\mu , \tag{19c}$$

where

$$\theta_\mu \equiv -\tan^{-1}\frac{\tan[\alpha_\mu \ln(k/2)+x_\mu]}{\tanh(\pi\alpha_\mu/2)} \tag{19d}$$

and

$$x_\mu \equiv \arg\Gamma(1-i\alpha_\mu) . \tag{19e}$$

The angular functions tend asymptotically to[25]

$$\phi_\mu(R,\alpha,\hat{\mathbf{r}}_1,\hat{\mathbf{r}}_2) \underset{r_1\to\infty}{\sim} r_1^{1/2}\sum_{ll'} P_{nl}(r_2)\mathcal{Y}_{ll'LM}(\hat{\mathbf{r}}_2,\hat{\mathbf{r}}_1) \times A_{(ll'),\mu} . \tag{20}$$

In Eq. (20), $P_{nl}(r_2)$ is the radial wave function for the $nl$ level of atomic hydrogen and $\mathcal{Y}_{ll'LM}(\hat{\mathbf{r}}_2,\hat{\mathbf{r}}_1)$ is defined by

$$\mathcal{Y}_{ll'LM}(\hat{\mathbf{r}}_2,\hat{\mathbf{r}}_1) \equiv \sum_{mm'} Y_{lm}(\hat{\mathbf{r}}_2)Y_{l'm'}(\hat{\mathbf{r}}_1)\langle lml'm'|LM\rangle . \tag{21}$$

Substituting Eqs. (18) and (20) in Eq. (14), we find that the wave function for the $LM$ partial wave tends asymptotically to

$$\psi^-_{ll'kLM}(\mathbf{r}_1,\mathbf{r}_2) \underset{r_1\to\infty}{\sim} i(r_1r_2)^{-1}(2\pi k)^{-1/2}\sum_{\bar{l}\bar{l}'} P_{n\bar{l}}(r_2)\mathcal{Y}_{\bar{l}\bar{l}'LM}(\hat{\mathbf{r}}_2,\hat{\mathbf{r}}_1)(e^{-i[kr_1-(1/2)\pi\bar{l}']}S^\dagger_{(\bar{l}\bar{l}'),(ll')}-\delta_{\bar{l}\bar{l}'}\delta_{ll'}e^{+i[kr_1-(1/2)\pi l']}) , \tag{22}$$

where the scattering matrix in the $(ll')$ basis is defined by

$$S^\dagger_{(\bar{l}\bar{l}'),(\bar{l}\bar{l}')} \equiv \sum_\mu e^{-i(1/2)\pi\bar{l}'}A_{(\bar{l}\bar{l}'),\mu}e^{-i\xi_\mu}\bar{S}^\dagger_\mu e^{-i\xi_\mu}A_{\mu,(ll')}e^{-i(1/2)\pi l'} \tag{23}$$

and where the scattering matrix in the adiabatic hyperspherical representation is diagonal and defined by

$$\bar{S}^\dagger_\mu \equiv e^{-2i\eta_\mu} . \tag{24}$$

#### 4. *The final- and initial-state wave functions*

In terms of the adiabatic hyperspherical basis functions that we calculate, our final-state wave function is obtained by substituting Eq. (14) into Eq. (13) to get

$$\psi^-_{nlm\mathbf{k}_P}(\mathbf{r}_2,\mathbf{r}_1) = k_P^{-1/2}\sum_{l'm'}\sum_{LM}\sum_\mu \psi^-_{\mu k_P}(R,\alpha,\hat{\mathbf{r}}_2,\hat{\mathbf{r}}_1)e^{-i\xi_\mu}A^\dagger_{\mu,(ll')}\langle LM|lml'm'\rangle Y^*_{l'm'}(\hat{\mathbf{k}}_P) , \tag{25}$$

where the hyperspherical channel function $\psi^-_{\mu k_P}$ is defined in Eq. (14b), the phase $\xi_\mu$ is defined in Eq. (19), and the matrix elements $A_{\mu,(ll')}$ are defined in Eq. (14a). Substituting Eq. (22) in Eq. (13), we may now verify the general boundary condition in Eq. (11),

$$\psi^-_{nlmk}(\mathbf{r}_1,\mathbf{r}_2) \underset{r_1\to\infty}{\sim} (2\pi)^{-3/2}r_2^{-1}P_{nl}(r_2)Y_{lm}(\hat{\mathbf{r}}_2)\exp(i\mathbf{k}\cdot\mathbf{r}_1)+(2\pi)^{-3/2}(r_1r_2)^{-1}\sum_{\bar{l}\bar{m}} P_{n\bar{l}}(r_2)Y_{\bar{l}\bar{m}}(\hat{\mathbf{r}}_2)f_{\bar{l}\bar{m},lm}(\mathbf{k}',\mathbf{k})e^{-ikr_1} , \tag{26}$$

where the scattering amplitude is defined by

$$f_{\bar{l}\bar{m},lm}(\mathbf{k}',\mathbf{k}) \equiv (2\pi i/k)\sum_{\bar{l}'\bar{m}'}\sum_{l'm'}\sum_{LM} Y_{\bar{l}'\bar{m}'}(\hat{\mathbf{r}}_1)\langle \bar{l}\,\bar{m}\,\bar{l}'\,\bar{m}'|LM\rangle \times e^{i(1/2)\pi\bar{l}'}(S^\dagger-1)^{(LM)}_{(\bar{l}\bar{l}'),(ll')}e^{i(1/2)\pi l'}Y^*_{l'm'}(\hat{\mathbf{k}})\langle lml'm'|LM\rangle \tag{27}$$

and where

$$\mathbf{k}' \equiv k\hat{\mathbf{r}}_1 . \tag{28}$$

Finally, we use the same initial-state wave function for $H^-$ that was used in the calculations of Park *et al.*,[16] namely,

$$\psi_0(\mathbf{r}_1,\mathbf{r}_2) = (R^{5/2}\cos\alpha\sin\alpha)^{-1}\phi_{\mu=0}(R,\alpha,\hat{\mathbf{r}}_1,\hat{\mathbf{r}}_2)F_{\mu=0}(R) , \tag{29}$$

where $\mu=0$ is the lowest adiabatic hyperspherical $^1S$ channel, $\phi_{\mu=0}$ becomes proportional as $r_1\to\infty$ to the H($1s$) wave function, and $F_{\mu=0}(R)$ is the lowest energy radial solution for the $\mu=0$ channel.[16]

### D. $H^-$ transition form factor

With Eqs. (25) and (29) for the final- and initial-state wave functions, we are now prepared to evaluate the $H^-$ transition form factor in Eq. (7). Note first that the adiabatic hyperspherical angle functions $\phi_\mu$ in Eqs. (14b) and (29) are normally calculated using an expansion in one-electron spherical harmonics,[25]

$$\phi_\mu=\sum_{l_1 l_2} g^\mu_{l_2 l_1}(R,\alpha)\mathcal{Y}_{l_2 l_1 LM}(\hat{\mathbf{r}}_2,\hat{\mathbf{r}}_1) , \tag{30}$$

where $\mathcal{Y}_{l_2 l_1 LM}$ is defined in Eq. (21) and where the total angular-momentum quantum number $L$ is appropriate for the channel $\mu$. Substituting Eqs. (14b), (25), (29), and (30) in Eq. (7), expanding the integrand in Eq. (7) in partial waves, and carrying out all angular integrations (over $\hat{\mathbf{r}}_1$ and $\hat{\mathbf{r}}_2$) analytically, we obtain

$$\epsilon^{H^-}_{nlm}(\mathbf{K},\mathbf{k}_P)=4\pi\sum_{l'm'}\sum_{LM}\sum_{\mu}(-1)^{l+l'+M}[L]^{-1/2}\begin{pmatrix} l & l' & L \\ m & m' & -M\end{pmatrix} Y_{l'm'}(\hat{\mathbf{k}}_P)Y^*_{LM}(\hat{\mathbf{K}})\exp(i\tfrac{1}{2}\pi L)$$

$$\times A_{(ll'),\mu}e^{i(\xi_\mu+\eta_\mu)}Q^L_{\mu 0}(K,k_P) , \tag{31}$$

where we have used the symbol $[x]\equiv 2x+1$ and where $Q^L_{\mu 0}$ is defined as[30]

$$Q^L_{\mu 0}(K,k)\equiv[L](4\pi k)^{-1/2}\int_0^\infty dR\, F_{\mu k_P}(R)F_0(R)I^L_{\mu 0}(K,R) . \tag{32}$$

In Eq. (32), $I^L_{\mu 0}(K,R)$ represents the integral over the hyperspherical angle $\alpha$,[31]

$$I^L_{\mu 0}(K,R)\equiv 2\sum_{l_1 l_2}[l_2]^{1/2}\begin{pmatrix} l_2 & L & l_1 \\ 0 & 0 & 0\end{pmatrix}(-1)^{l_2}\int_0^{\pi/4} d\alpha\, g^0_{l_1 l_1}(R,\alpha)[g^\mu_{l_1 l_2}(R,\alpha)j_L(KR\sin\alpha)+g^\mu_{l_2 l_1}(R,\alpha)j_L(KR\cos\alpha)] . \tag{33}$$

### E. Calculation of $J_{nl}(K,k_P,\theta_P)$

The function $J_{nl}$, defined in Eq. (6), is needed to compute the doubly differential cross sections in Eq. (4). It is calculated by taking the absolute square of the $H^-$ form factor in Eq. (31), summing over the magnetic quantum number $m$ of the final state of the H atom, and integrating over the azimuthal scattering angle $\phi$. We indicate here briefly the many steps involved in doing this calculation. First, when Eq. (31) is squared, one obtains products of spherical harmonics having the same arguments. One rewrites these products as a linear combination of single spherical harmonics with the same angular argument.[32] Second, one is then able to sum over the magnetic quantum numbers $m'$ and $M$ in Eq. (31) [as well as the corresponding ones in the complex conjugate of Eq. (31)] using a standard relation for the sum over four $3j$ symbols; one obtains an expression having a summation over a dummy angular momentum $a$ and its magnetic quantum number, $m_a$.[33] Third, summation over $m_a$ and $m$ may then be carried out using a standard orthogonality relation for $3j$ symbols.[34(a)] Fourth, summation over $a$ may then be performed using a standard sum rule for $6j$ coefficients.[34(b)] Finally, one may then employ the spherical-harmonic addition theorem.[35] The result is

$$\sum_m|\epsilon^{H^-}_{nlm}(\mathbf{K},\mathbf{k}_P)|^2=(-1)^l\sum_{l'\bar{l}'}\sum_{L\bar{L}}\sum_{\Lambda}[\Lambda]\begin{Bmatrix}\bar{l}' & l' & \Lambda \\ L & \bar{L} & l\end{Bmatrix}\begin{pmatrix} l' & \bar{l}' & \Lambda \\ 0 & 0 & 0\end{pmatrix}\begin{pmatrix} L & \bar{L} & \Lambda \\ 0 & 0 & 0\end{pmatrix}P_\Lambda(\hat{\mathbf{k}}_P\cdot\hat{\mathbf{K}})X_{ll'L}(K,k_P)X_{\bar{l}\bar{l}'\bar{L}}(K,k_P) , \tag{34}$$

where $P_\Lambda$ is a Legendre polynomial and the coefficients $X_{ll'L}$ are defined by

$$X_{ll'L}(K,k_P)\equiv(-1)^{l'+L}[l']^{1/2}\exp(i\tfrac{1}{2}\pi L)\sum_\mu A_{(ll'),\mu}\exp[i(\xi_\mu+\eta_\mu)]Q^L_{\mu 0}(K,k_P) . \tag{35}$$

In the special case of $H(nlm)=H(1s)$, Eq. (34) reduces to the absolute square of Eq. (29) of Ref. 16.

Performing now the integral over the azimuthal angle $\phi$ in Eq. (6), we obtain finally

$$J_{nl}(K,k_P,\theta_P)=\sum_\Lambda[\Lambda]I_\Lambda(K,\theta_P)M_\Lambda(l,K,k_P) , \tag{36}$$

where

$$I_\Lambda(K,\theta_P)\equiv\frac{1}{2\pi}\int_0^{2\pi}P_\Lambda(\hat{\mathbf{K}}\cdot\hat{\mathbf{k}}_P)d\phi \tag{37}$$

and

$$M_\Lambda(l,K,k_P)\equiv(-1)^l\sum_{l'\bar{l}'}\sum_{L\bar{L}}\begin{Bmatrix}\bar{l}' & l' & \Lambda \\ L & \bar{L} & l\end{Bmatrix}\begin{pmatrix} l' & \bar{l} & \Lambda \\ 0 & 0 & 0\end{pmatrix}\begin{pmatrix} L & \bar{L} & \Lambda \\ 0 & 0 & 0\end{pmatrix}X_{ll'L}X^\dagger_{\bar{l}\bar{l}'\bar{L}} . \tag{38}$$

In our calculations we include $^1S$, $^1P$, and $^1D$ partial waves, so that $0 \le L, \bar{L} \le 2$, and hence $0 \le \Lambda \le 4$. The evaluation of the integrals $I_\Lambda$ is carried out using an addition theorem for Legendre functions.[36] The result is

$$I_\Lambda(K,\theta_P) = P_\Lambda(\zeta) P_\Lambda(\cos\theta_P) , \tag{39}$$

where $\zeta$ is the $z$ component of the momentum-transfer unit vector $\hat{\mathbf{K}}$ [cf. Eq. (5)]

$$\zeta \equiv \frac{k_i - k_f \cos\theta_f}{K} = \frac{k_i^2 - k_f^2 + K^2}{2k_i K} \doteq \frac{K}{2k_i} + \frac{K_{\min}}{K} . \tag{40}$$

Note that $\mathbf{k}_i$, the momentum of the incident $H^-$ projectile, has been chosen as the $z$ axis, and $\mathbf{k}_f$ is the final momentum of the $H(n=2)$-$e^-$ system.

### F. The laboratory-frame doubly and singly differential cross sections

The Galilean invariant DDCS may now be expressed in terms of Legendre functions of $\cos\theta_P$ by substituting Eqs. (36) and (39) into Eq. (4b) to get

$$\Sigma^G_{nl}(k_P,\theta_P) \equiv \sum_{\Lambda=0}^{4} [\Lambda] A_\Lambda(nl,k_P) P_\Lambda(\cos\theta_P) , \tag{41}$$

where

$$A_\Lambda(nl,k_P) \equiv \frac{8\pi}{v_i^2} \int_{K_{\min}(0)}^{K_{\max}(0)} P_\Lambda(\zeta) M_\Lambda(l,K,k_P) \times |\epsilon^{\mathrm{He}}_{00}(K) - 2|^2 \frac{dK}{K^3} + \frac{8\pi}{v_i^2} \int_{K_{\min}(\bar{I}_{\mathrm{He}})}^{K_{\max}(\bar{I}_{\mathrm{He}})} P_\Lambda(\zeta) M_\Lambda(l,K,k_P) \times S^{\mathrm{He}}_{\mathrm{inc}}(K) \frac{dK}{K^3} . \tag{42}$$

The laboratory- and the projectile-frame DDCS's are then obtained easily from Eqs. (8) and (10).

The laboratory-frame singly differential cross section (giving the angular distribution of detached electrons) is then calculated as

$$\left[\frac{d\sigma}{d\omega}\right]_L \equiv \int \left[\frac{d\sigma}{d\omega\, dE}\right]_L dE_L = \int_{k_L^{\min}}^{k_L^{\max}} dk_L k_L^2 \Sigma^G_{nl}(k_P(k_L,\theta_L),\theta_P(k_L,\theta_L)) , \tag{43}$$

where $dE_L = k_L dk_L$.

## III. RESULTS

### A. Numerical matters

Many of the numerical details of these calculations are presented in the doctoral theses of Park[37] and Liu[38] as well as in the article by Park *et al.*[16,19] In particular, the values for $K_{\max}$ and $K_{\min}$ in Eq. (42) are calculated as in Sec. III B of Ref. 16 except that in our calculations the binding energy of $H^-$ must also take into account the energy for excitation of $H(n=2)$. As in Ref. 16, we employ an average binding energy for the helium target $\bar{I}_{\mathrm{He}}$ equal to 35 eV. However, we also illustrate below the sensitivity of our results to this value. In our calculations, six adiabatic hyperspherical channels $\mu$ were included (as discussed in detail in Ref. 4): $\mu = {}^1S(K=\pm1)$, ${}^1P\pm$, ${}^1P(pd)$, and ${}^1D+$. Finally, the phase shifts $\eta_\mu$ for the $\mu$th adiabatic hyperspherical channel, which are defined by Eqs. (18) and (19), may be calculated accurately by using the known analytic asymptotic behavior of the regular and irregular Bessel functions.[39] Specifically, the solutions of Eq. (15) in the asymptotic region [for which the effective potential is given by Eq. (17)] may be represented as a linear superposition of $z^{1/2}J_\nu(z)$ and $z^{1/2}Y_\nu(z)$, where $z \equiv kR$, $\nu \equiv \lambda_\mu + \frac{1}{2}$, and $J_\nu(z)$ and $Y_\nu(z)$ are the regular and irregular Bessel functions, whose asymptotic forms are given by Eqs. (9.2.5), (9.2.6), (9.2.9), and (9.2.10) of Ref. 39.

### B. Projectile-frame DDCS for 0.5-MeV $H^- + He \to H(n=2) + e^- + He^*$

In Ref. 4 we discussed in detail the influence of each of the six adiabatic hyperspherical channels $\mu$ included in our calculations on the projectile- and laboratory-frame DDCS's defined in Eqs. (8) and (10). Briefly, the $\mu = {}^1P+$ channel has a large shape resonance just above threshold which dominates the low-energy projectile-frame DDCS. This channel, however, has a real value for the effective angular-momentum $\lambda_\mu$ [cf. Eq. (17)], so that its detachment cross section is zero at threshold.[4] Three of the other eigenchannels, however, have attractive long-range dipole potentials corresponding to complex values of $\lambda_\mu$.[4] Hence the threshold value of the DDCS due to these channels, while small, is nevertheless nonzero in the projectile frame. Since

$$\left[\frac{d\sigma}{d\omega\, dE}\right]_L = \left[\frac{k_L}{k_P}\right] \left[\frac{d\sigma}{d\omega\, dE}\right]_P , \tag{44}$$

a finite value for $(d\sigma/d\omega\, dE)_P$ for $k_P = 0$ leads to a cusp in the laboratory-frame DDCS. Reference 4 discussed these effects on the forward-direction DDCS in both the projectile and laboratory frames. Here we present a more complete picture of the angular distribution for the DDCS in both frames.

Our result for the projectile-frame DDCS for process (1) is presented in Fig. 1. The dominant feature of the DDCS is the peak just above threshold due to the ${}^1P+$ shape resonance.[4] As found experimentally,[11(f),11(h)] the angular distribution of the DDCS in the projectile frame is close to being isotropic.

This isotropic angular distribution may be understood as a result of a cancellation in one of the relevant integrals over the momentum transfer $K$, as follows. First if we ignore all channels other than the dominant ${}^1P+$ channel, then only the coefficients $A_\Lambda$ for $\Lambda = 0$ and 2 contribute to the Galilean invariant cross section in Eq. (41). This result follows from the observation that the absolute square of the sum of ${}^1P$ partial-wave transition amplitudes $X_{ll'L}$ for $L = 1$ [cf. Eq. (35)] only contributes to

the coefficients $M_\Lambda$ in Eq. (38) for the cases $\Lambda=0$ and 2 [due to the $3j$ symbol involving $L$, $\bar{L}$, and $\Lambda$ in Eq. (38)]. Second, $P_\Lambda(\zeta)$ for $\Lambda=2$ causes a cancellation in the second (and usually largest) integral in Eq. (42) for $A_{\Lambda=2}$. This result may be understood as follows. In the collision of interest here, small momentum transfers dominate, so that Eq. (40) reduces to $\zeta \approx K_{\min}/K$. But $P_2(K_{\min}/K)$ changes sign at $K \approx 3^{1/2}K_{\min}$, which is just above the value of $K$ at which the remaining part of the second integrand in Eq. (42), $M_2 S^{\mathrm{He}}_{\mathrm{inc}}(K)/K$, has its maximum value, thereby causing a large cancellation in the second integral in Eq. (42) for $\Lambda=2$. [The first integral in Eq. (42) for $\Lambda=2$ gives an order of magnitude smaller contribution to the Galilean-invariant cross section in Eq. (41) than does the $\Lambda=0$ term.] Hence, for the collision of interest here, the isotropic part of the DDCS is dominant. Note, however, that since $K_{\min}$ is sensitive to the average excitation energy of the target atom, this cancellation and hence the resulting isotropic angular distribution of the projectile-frame DDCS in the neighborhood of $^1P+$ resonance may not occur for $H^-$ collisions with other targets. We are currently investigating the DDCS for $H^-$ detachment collisions on other rare-gas targets in order to elucidate this matter further.

Figure 1 also indicates how the projectile-frame DDCS affects the features observed experimentally in the laboratory frame. For a fixed angle $\theta_L$ in the laboratory, detached electrons are detected having a range of kinetic energies $\frac{1}{2}k_L^2$ according to the kinematic Eq. (9). These allowed values of laboratory-frame kinetic energies lie on a trajectory in the projectile frame, as illustrated in Fig. 1 for the laboratory angles $\theta_L=0.3°$, 0.5°, and 0.7°. [Note that in the projectile frame, the He target is the "incident" particle and its direction determines the positive $z$ axis with respect to which $\theta_P$ is measured. Hence in the laboratory frame, $\theta_P=0°$ corresponds to lower detached electron energies than does $\theta_P=180°$. These purely kinematic relationships are illustrated in Fig. 2, in which we have plotted $k_P$ and $\theta_P$ as functions of $E_L$ ($=\frac{1}{2}k_L^2$) and $\theta_L$.] Figure 1 shows that for $\theta_L=0.3°$, there should be two $^1P+$ shape-resonance peaks in the laboratory frame (with the higher-energy peak slightly greater in magnitude than the lower-energy peak). For $\theta_L=0.3°$ the tra-

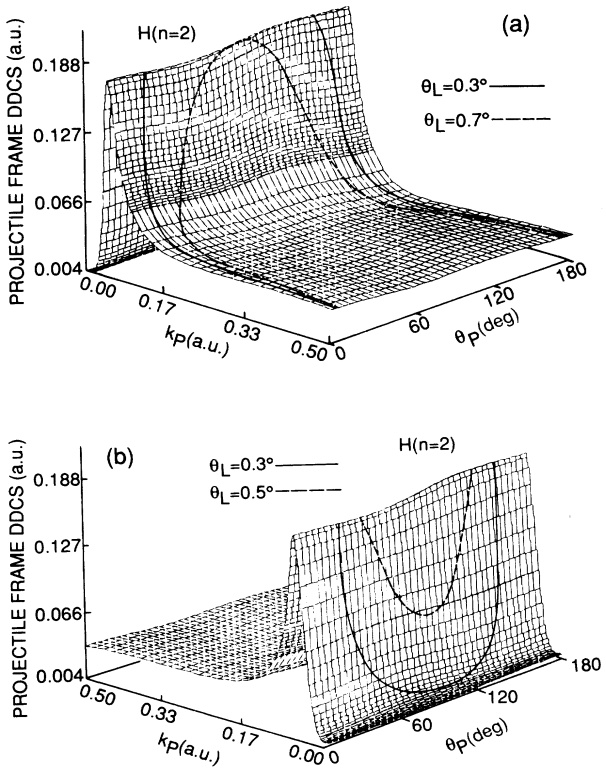


FIG. 1. Doubly differential cross section (DDCS) for electron detachment vs electron momentum $\mathbf{k}_P \equiv (k_P, \theta_P)$ in the projectile ($P$) frame. (a) and (b) show the high- and the low-energy sides, respectively, of the $^1P+$ shape-resonance peak in the DDCS. The $\theta_L=0.3°$ and 0.7° trajectories in (a) and the $\theta_L=0.3°$ and 0.5° trajectories in (b) on the DDCS surface trace the projectile-frame DDCS contributions to the laboratory-frame DDCS as a function of electron momentum $k_L$ in the laboratory for fixed laboratory angles $\theta_L$. The results shown employ an effective excitation energy $\bar{I}_{\mathrm{He}}$ of 35 eV for the helium target. Note that the DDCS is small but finite for $k_P=0$.

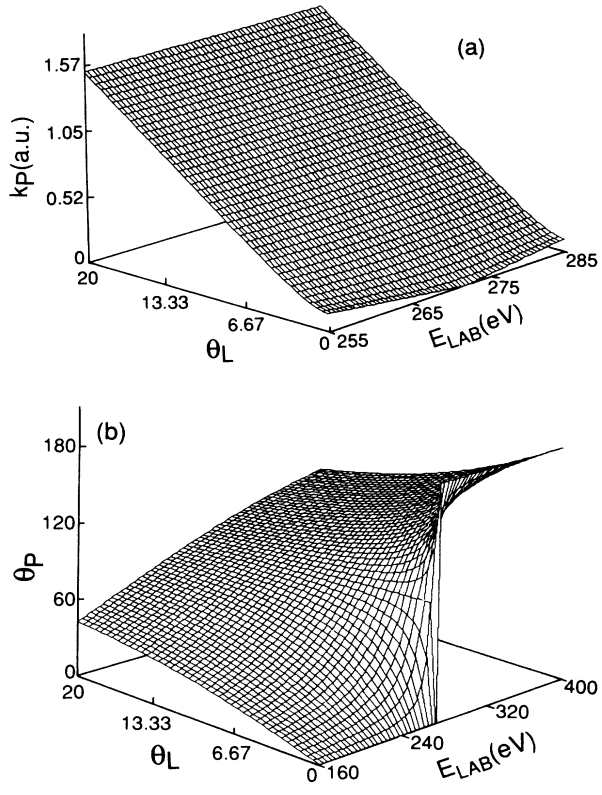


FIG. 2. Kinematic relationship of the detached-electron momentum $\mathbf{k}_P \equiv (k_P, \theta_P)$ in the projectile frame to the corresponding momentum $\mathbf{k}_L \equiv (k_L, \theta_L)$ in the laboratory frame according to Eq. (9). (a) $k_P(E_L, \theta_L)$, where $E_L \equiv \frac{1}{2}k_L^2$. (b) $\theta_P(E_L, \theta_L)$.

jectory in Fig. 1 crosses the value of $k_P$ at which the $^1P+$ shape resonance occurs but never samples $k_P=0$; only $\theta_L=0.0°$ does that. Hence only at $\theta_L=0.0°$ does one get a cusp singularity due to the finite DDCS at $k_P=0$ in the projectile frame, as discussed in Ref. 4. Figure 1(b) shows that the trajectory for $\theta_L=0.5°$ does not extend to as small values of $k_P$ as does $\theta_L=0.3°$. Hence while the $^1P+$ shape-resonance peaks in the laboratory frame should be approximately the same magnitude for both $\theta_L=0.3°$ and 0.5°, the minimum value of the DDCS between the peaks should be of much greater magnitude for 0.5° than for 0.3°.

As shown in Fig. 1(a), for $\theta_L=0.7°$ the trajectory just reaches the top of the $^1P+$ shape resonance, thereby indicating that for all angles $\theta_L \geq 0.7°$ only a single peak due to the $^1P+$ shape resonance will be observed in the laboratory. Actually, the critical angle at which the double-peak structure in the laboratory frame changes to a single-peak structure is highly dependent on the energy location of the $^1P+$ shape resonance in the projectile frame. In our adiabatic hyperspherical calculations, as well as in those of Lin,[28] this resonance is predicted to occur at about 40 meV above threshold. More accurate calculations[3(a),40] show that the resonance occurs at about 18 meV above threshold; this is consistent with experimental measurements.[41] Kinematic considerations predict that for a resonance peak at 18 meV, the double-peak to single-peak transition in the laboratory frame will occur for $\theta_L \approx 0.47°$. This was shown in the semiempirical calculations of Maleki and Macek.[14] We conclude that laboratory measurements of the DDCS for $H^-$ detachment as a function of $\theta_L$ provide a very sensitive determination of the location of the $^1P+$ shape-resonance peak for the $H(n=2)$-$e^-$ three-body system.

### C. Laboratory-frame DDCS for 0.5-MeV $H^-+He \rightarrow H(n=2)+e^-+He^*$

The qualitative features of the laboratory-frame DDCS for process (1), discussed above in connection with the structure of the projectile-frame DDCS, are shown here quantitatively. Figure 3 shows the DDCS for producing $H(n=2)$ for five laboratory-frame angles $\theta_L$. As expected on the basis of the above discussion, we see that for $\theta_L=0.0°$ there is not only the double-peaked structure due to the $^1P+$ shape resonance but also a cusp in the cross section at the equal-velocity position ($\approx$272 eV). This cusp behavior is not evident in the $\theta_L=0.3°$ curve; instead there is a local minimum in the cross section at the equal-velocity position. This minimum rises as $\theta_L$ increases (cf. the $\theta_L=0.4°$ curve) until it disappears at $\theta_L=0.7°$, leaving only a single peak at the equal-velocity position due to the $^1P+$ shape resonance. This single peak diminishes rapidly as $\theta_L$ increases further (cf. the $\theta_L=1.0°$ curve).

In order to analyze the angular dependence of the cusp feature, we show in Fig. 4 our results for the DDCS *ignoring the* $^1P+$ *shape-resonance channel.* For $\theta_L=0.0°$, the laboratory-frame DDCS is singular. For $\theta_L \geq 4.0°$, however, there is still a peak at the equal-velocity position arising from division of the finite DDCS in the projectile frame by $k_P$ for small values of $k_P$ [cf. Eq. (44)]. For $\theta_L > 0.8°$, however, this cusp feature disappears.

Our predictions for the separate $H(2p)$ and $H(2s)$ cross sections for process (1) are presented in Fig. 5 for four values of $\theta_L$. While our predictions for $\theta_L=0°$ show cusps at the equal-velocity position,[4] the results in Fig. 5 for angles $\theta_L \geq 0.3°$ show no sign of any cusp features, as is to be expected from the results shown in Fig. 4. We observe that the cross sections for $H(2p)$ achieve magnitudes that are factors of 2–4 greater than those for $H(2s)$. By $\theta_L=4.0°$, however, these cross sections are both essentially zero.

Our predictions for the $H(2p)$ cross section may be compared with the experimental measurements of Menendez and Duncan,[11(g)] who measured the DDCS for process (1) at $\theta_L=0°$ in coincidence with Lyman-$\alpha$ photons from the decay of $H(2p)$. Their results, shown in

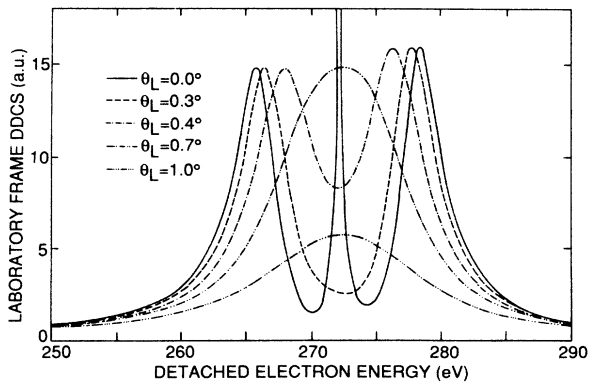


FIG. 3. Laboratory-frame DDCS's for detachment plus excitation of $H(n=2)$ vs detached-electron kinetic energy for the five fixed-electron ejection angles $\theta_L=0.0°$, 0.3°, 0.4°, 0.7°, and 1.0°.

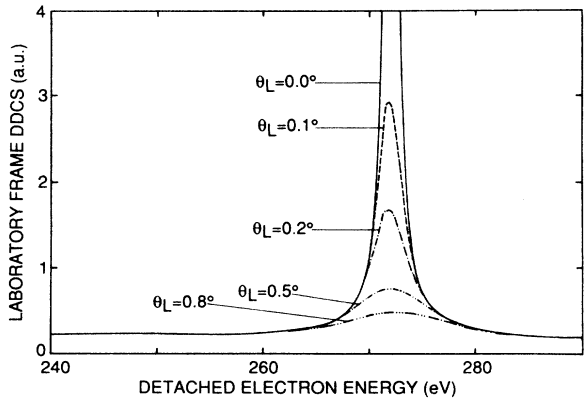


FIG. 4. Angular dependence of the cusp feature in the laboratory-frame DDCS's for detachment plus excitation of $H(n=2)$. These DDCS's have been calculated omitting the $^1P+$ shape-resonance channel in order to display clearly the cusp feature at the equal-velocity position. They are plotted vs the detached-electron kinetic energy for the five fixed-electron ejection angles $\theta_L=0.0°$, 0.1°, 0.2°, 0.5°, and 0.8°.

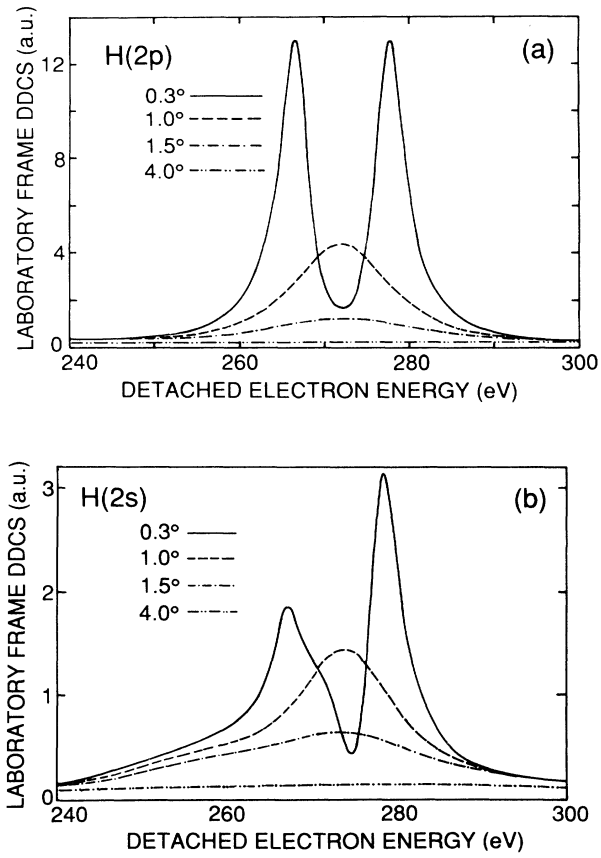


FIG. 5. Laboratory-frame DDCS's for detachment plus excitation of H($2p$) and H($2s$) vs detached-electron kinetic energy for the four fixed-electron ejection angles $\theta_L = 0.3°$, 1.0°, 1.5°, and 4.0°. (a) DDCS for H($2p$). (b) DDCS for H($2s$).

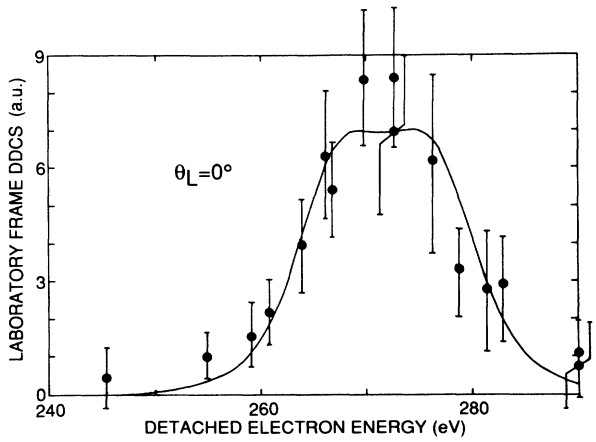


FIG. 6. Comparison between the experiment of Menendez and Duncan [Ref. 11(g)] for the energy spectrum of detached electrons at $\theta_L = 0°$ in coincidence with Lyman-$\alpha$ photons from the excitation and subsequent decay of H($2p$) resulting from process (1) and our theoretical predictions for the DDCS for H($2p$) in the laboratory frame as folded with the experimental angular and energy convolution functions.

Fig. 6, do not show the cusp or $^1P+$ shape-resonance features we have predicted[4] for $\theta_L = 0°$. However, their results have an energy resolution of $\Delta E_L / E_L = 0.02$ and an angular resolution of $\Delta\theta_L = 0.85°$ which must be taken into account.[11(g),42] When we fold our theoretically predicted DDCS's for detachment plus excitation to H($2p$) with the experimental energy and angular convolution functions,[42] we obtain the result shown by the solid curve in Fig. 6. Agreement with the experimental results is excellent.

### D. Comparison with experiments for 0.5-MeV $H^- + He \rightarrow H^* + e^- + He^*$

The key discrepancy between the experimental measurements[11(b)–(d)] for process (2), in which the state of excitation of the H-atom final state is not measured, and the theoretical calculations[12–16] for process (3), in which the H-atom final state is assumed to be H($1s$), is that the experimental values for the higher-energy peak are much greater than those predicted theoretically for $\theta_L \leq 4.0°$. This apparent evidence of the importance of excited final states of the H atom may now be verified by adding our current results for process (1), in which the H-atom final state is assumed to be H($n = 2$), to the previous results of Park *et al.*[16,19] for process (3), in which only the H($1s$) final state is taken into account. We have recalculated the DDCS's for process (3) according to Ref. 16 and have included all corrections.[19] The results are shown in Fig. 7. One sees clearly the double-peaked structure for $\theta_L \leq 4.0°$ due to an interference of $s$ and $p$ partial waves.[12,14,16]

We compare our present results for processes (1) and (3) with experimental results[11(b)] for process (2) in Fig. 8. The dashed line shows our predictions for leaving the hydrogen atom in H($1s$), the dashed-dotted line shows the results for leaving it in H($n = 2$), and the solid line gives the sum of these results. The triangles show the relative experimental measurements, which include all possible

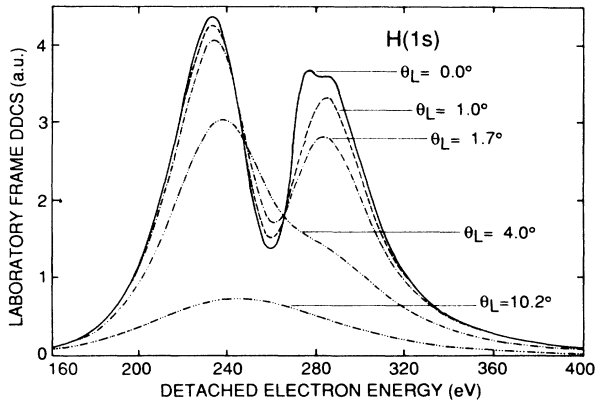


FIG. 7. Laboratory-frame DDCS's for process (3) vs electron kinetic energy for the five fixed detached-electron ejection angles, $\theta_L = 0.0°$, 1.0°, 1.7°, 4.0°, and 10.2°.

final states for the H atom. The relative experimental results were normalized to our solid curve at the energy of the lower-energy peak. The comparison for $\theta_L = 0.3°$ shows that the experimental resolution is not sufficient to resolve the $^1P+$ shape-resonance features centered about the equal-velocity energy. Clearly, however, the magnitude of these predicted features explains much of the previous discrepancy between experiment and the calculations which included only the H($1s$) final state.[12–16] The comparison for $\theta_L = 1.5°$ is more straightforward since the structure due to the $^1P+$ shape-resonance channel has disappeared at this relatively large laboratory-frame angle (cf. Fig. 5). Clearly, experiment is in much better agreement with the present theoretical predictions, which include the H($n=2$) states. Whether the remaining discrepancies are due primarily to the experimental angular resolution, which may permit sampling of the much larger cross sections at smaller angles, or due primarily to the theoretical neglect of H($n=3$) and higher final states of the H atom, is an open question.

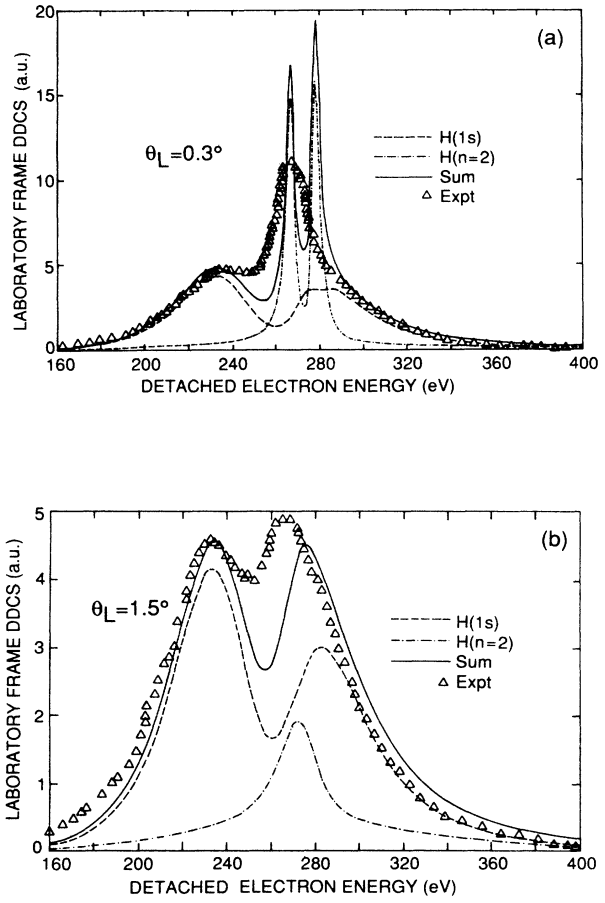


FIG. 8. Laboratory-frame DDCS's vs detached-electron kinetic energy at two fixed detached-electron ejection angles: (a) $\theta_L = 0.3°$ and (b) $\theta_L = 1.5°$. — — —, present theoretical predictions for 0.5-MeV $H^- + He \rightarrow H(1s) + e^- + He^*$; —·—·—, present theoretical predictions for 0.5-MeV $H^- + He \rightarrow H(n=2) + e^- + He^*$; ——, sum of the present theoretical predictions for H($1s$) and H($n=2$) final states; △, relative experimental measurements of Menendez and Duncan [Ref. 11(b)] for 0.5-MeV $H^- + He \rightarrow H^* + e^- + He^*$, where $H^*$ includes H($1s$) as well as all excited states. Experiment is normalized to the solid theoretical curve at the energy position of the lower-energy peak.

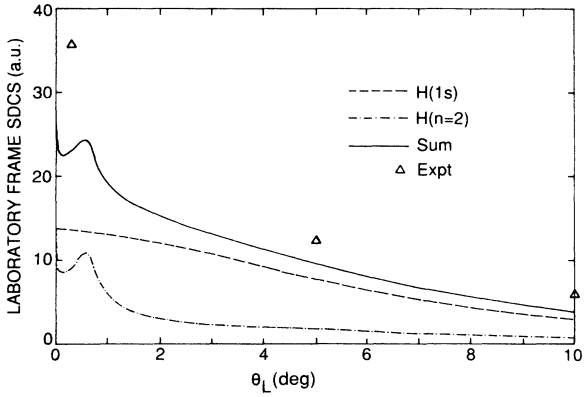


FIG. 9. Singly differential cross section (SDCS) for electron detachment vs detached-electron scattering angle in the laboratory frame. Curves and symbols defined as in Fig. 8.

Figure 9 shows a similar comparison of experiment[11(b)] with our results for the singly differential cross section (SDCS), which is calculated according to Eq. (43). Our present calculations for process (3) (dashed curve), for process (1) (dashed-dotted curve), and for the sum (solid curve) are compared with the experimental data for process (2), which do not distinguish the final state of the H atom. These experimental measurements for the SDCS are absolute.[11(b)] The peak in the theoretically calculated H($n=2$) results for $0 < \theta_L < 1°$ is due to the $^1P+$ shape resonance. The H($n=2$) results also are singular at $\theta_L = 0°$ due to the cusp behavior of the DDCS at this angle. The solid curve representing the sum of the theoretical predictions for H($1s$) and H($n=2$) is 20%–30% below the measured SDCS for $\theta_L > 4°$, which *may* be due in part to inclusion of excited H-atom states with $n > 2$ in the experimental measurements. However, it may also be due in part to our use of a fixed average excitation energy for the helium target, as discussed in Sec. IV. The discrepancy between theory and experiment for $\theta_L \approx 0°$ may also require a detailed analysis of the experimental angular resolution due to the cusp singularity for $\theta_L = 0°$. This may explain the sharp rise in the experimental measurement near 0°. Clearly the present results give significantly improved agreement with experiment due to our inclusion of H($n=2$) final states.

## IV. DISCUSSION AND CONCLUSIONS

### A. Gailitis-Damburg oscillations

In Ref. 4 we presented the first quantitative predictions of the expected Gailitis-Damburg[2] oscillations in the DDCS's for excitation of H($n=2$). These oscillations are an effect of the long-range dipole field seen by the de-

tached electron due to the degeneracy of H($2p$) and H($2s$).[2] As shown in Fig. 5 of Ref. 4, these expected oscillations can only be observed for detached-electron energies of a few meV or less in the projectile frame due to the obscuring effect of the strong $^1P+$ shape resonance, which peaks at 18 meV.

We point out here that the predicted oscillations in our calculations are due to rapid variation of the analytic phase $\theta_\mu$ [cf. Eq. 19(d)] for those adiabatic hyperspherical channels $\mu$ having complex values of the effective angular-momentum $\lambda_\mu$ [cf. Eq. (17)]. Because of the attractive dipole field, these channels have finite cross sections at threshold in the projectile frame.[4] This analytic phase $\theta_\mu$ appears explicitly in the phase factor included in the transition amplitudes [cf. Eqs. 19(c) and (35)]. Figure 10 shows the rapid variation of the analytic phase $\theta_\mu$ for the three hyperspherical channels $\mu = {}^1S(K=+1)$, $^1P-$, and $^1D+$, all of which correspond to complex values of $\lambda_\mu$. These $\theta_\mu$'s vary rapidly over a very small range of the detached electron momentum $k$ near the detachment threshold.

The long-range dipole field also induces rapid oscillations in the effective normalization of the final-state wave function for the H($n=2$)-$e^-$ system. These additional oscillations may be extracted using generalized quantum defect theory by representing our adiabatic hyperspherical radial wave functions as[43]

$$F_{\mu k}(R) = N_\mu(k) F^0_{\mu k}(R) , \tag{45}$$

where the normalization factor $N_\mu(k)$, defined in the Appendix, describes most of the variation with $k$ of $F_{\mu k}(R)$ and where $F^0_{\mu k}(R)$ is a more smoothly varying function of $k$. Figure 11 shows the oscillatory behavior of $N_\mu(k)$ for the three adiabatic channels $\mu = {}^1S(K=+1)$, $^1P-$, and $^1D+$. While the oscillations for the $^1D+$ channel are large, this channel gives the smallest contribution to the DDCS for small values of $k$. The oscillation amplitudes for the $\mu = {}^1P-$ and $^1S(K=+1)$ channels are of the order of only tenths of a percent of the average amplitude. Thus, none of these oscillations contributes visibly to the Gailitis-Damburg oscillations shown in Fig. 5 of Ref. 4; those oscillations are due entirely to the rapid changes in the analytic phase $\theta_\mu$ shown in Fig. 10.

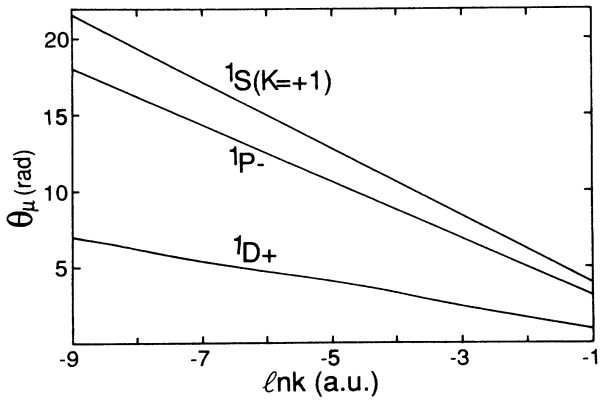


FIG. 10. Analytic phase $\theta_\mu$ [defined in Eq. 19(d)] vs ln$k$, where $k$ (a.u.) is the detached-electron momentum in the projectile frame, for the three adiabatic hyperspherical channels $\mu = {}^1S(K=+1)$, $^1P-$, and $^1D+$.

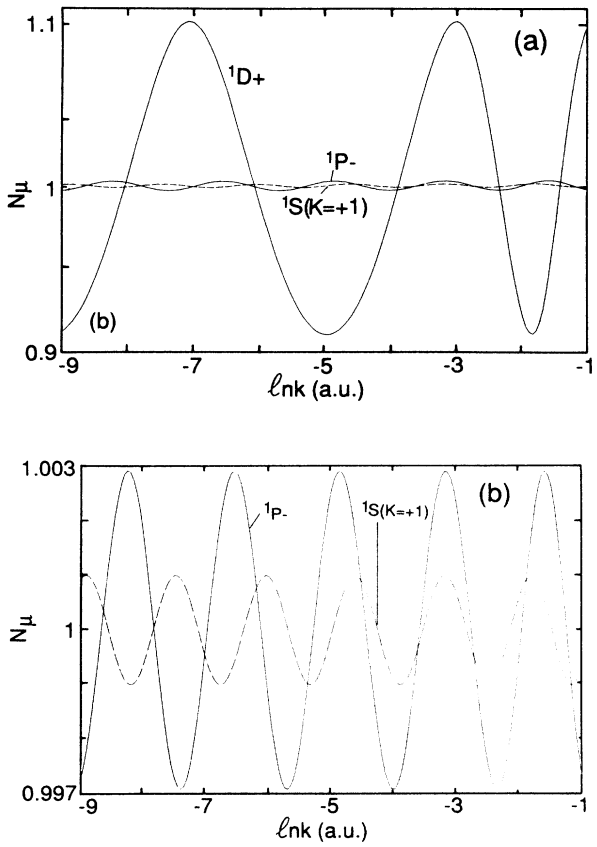


FIG. 11. (a) Normalization factors $N_\mu(k)$ [cf. Eq. (45)] for the three adiabatic hyperspherical channels $\mu = {}^1S(K=+1)$, $^1P-$, and $^1D+$ vs ln$k$, where $k$ is the detached-electron momentum in the projectile frame. (b) Same as (a) but with an enlarged vertical scale to show more clearly the oscillations in $N_\mu(k)$ for $\mu = {}^1S(K=+1)$ and $^1P-$.

### B. Sensitivity of the DDCS's to $\bar{I}_{\rm He}$

The commonly used closure approximation, which is employed to simplify the summation over the He target states, introduces a dependence of the theoretical calculations on the parameter $\bar{I}_{\rm He}$, the average excitation energy of the He target. There are a number of prescriptions for choosing $\bar{I}_{\rm He}$: one suggests setting $\bar{I}_{\rm He}$ equal to the energy needed to excite the lowest excited state;[44] another suggests the use of an angle-dependent $\bar{I}_{\rm He}$.[24] For the small angles of interest in the present calculations, we have followed Wright *et al.*[45] and Park *et al.*[16] and used $\bar{I}_{\rm He} = 35$ eV in the present work. We examine here the sensitivity of our results to this choice.

Figure 12(a) shows the laboratory-frame DDCS for process (3), in which the hydrogen atom is left in the 1$s$ final state, for four values of $\bar{I}_{\rm He}$ and for $\theta_L = 1.5°$. One observes a significant sensitivity of the magnitude of the

DDCS on $\bar{I}_{He}$: the smaller the value of $\bar{I}_{He}$, the larger the value of the DDCS. Furthermore, the location of the lower-energy peak shifts to lower energies as $\bar{I}_{He}$ increases. The location of the higher-energy peak, on the other hand, is relatively insensitive to the value of $\bar{I}_{He}$. We have chosen $\bar{I}_{He}=35$ eV since for this value the location of the lower-energy peak coincides with that measured experimentally. Note that the relative experimental results shown in Fig. 12 are normalized to our calculated DDCS for $\bar{I}_{He}=35$ eV at the energy of the lower-energy peak.

Figure 12(b) shows the laboratory-frame DDCS for process (1), in which the hydrogen atom is left in the $n=2$ state, for the same four values of $\bar{I}_{He}$ and for $\theta_L=1.5°$. One observes a much weaker sensitivity of the magnitude of the DDCS on $\bar{I}_{He}$. As expected, there is no

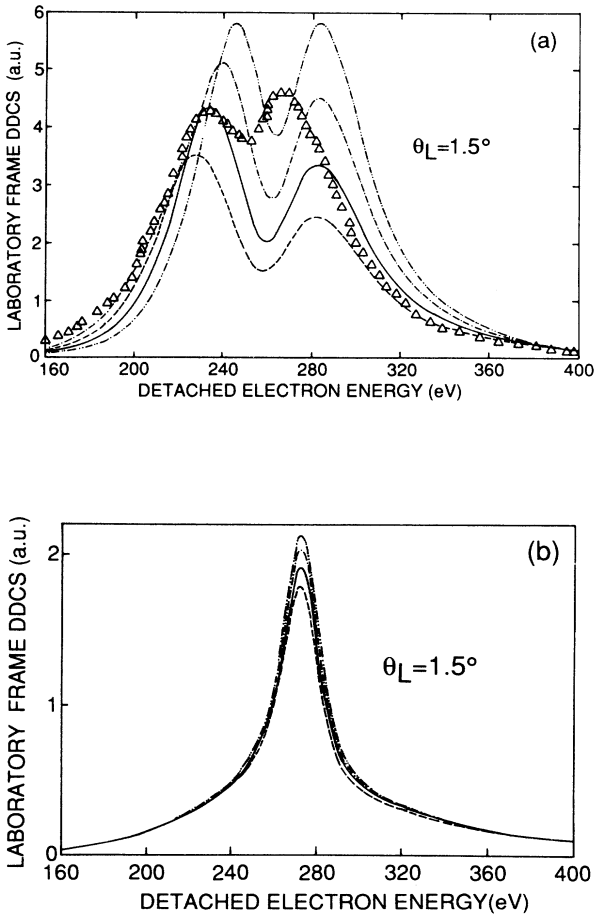


FIG. 12. Dependence of theoretically calculated DDCS's on $\bar{I}_{He}$, the average excitation energy of the He target for $\theta_L=1.5°$. $-\cdots-$, $\bar{I}_{He}=21$ eV; $-\cdot-\cdot-\cdot-$, $\bar{I}_{He}=28$ eV; ——, $\bar{I}_{He}=35$ eV; — — —, $\bar{I}_{He}=42$ eV. (a) DDCS's for 0.5-MeV $H^-+He\rightarrow H(1s)+e^-+He^*$. The triangles are the relative experimental measurements of Menendez and Duncan [Ref. 11(b)] for 0.5-MeV $H^-+He\rightarrow H^*+e^-+He^*$, where $H^*$ includes $H(1s)$ as well as all excited states. (b) DDCS's for 0.5-MeV $H^-+He\rightarrow H(n=2)+e^-+He^*$.

significant sensitivity of the energy position of these DDCS's for projectile excitation on the target parameter $\bar{I}_{He}$.

The difference in sensitivity of the $H(1s)$ and $H(n=2)$ DDCS's can be understood as follows: As discussed in detail by Macek *et al.*,[11(c)] the DDCS for $H(1s)$ is governed by an interference of $s$ and $p$ partial waves whose magnitude is proportional to $K_{min}$, the minimum value of the momentum transfer. Furthermore, $K_{min}$ is very sensitive to $\bar{I}_{He}$. On the other hand, since the DDCS for $H(n=2)$ is not governed by interferences of the various partial waves, its sensitivity to $K_{min}$ is greatly reduced. Furthermore, the large excitation energy of the $H(n=2)$ state reduces the sensitivity of $K_{min}$ on the value of $\bar{I}_{He}$.

In summary, we believe the value $\bar{I}_{He}=35$ eV to be the best one to use for the small electron-detachment angles of interest in these detachment collisions. For larger angles, however, an angular dependence for $\bar{I}_{He}$ may be appropriate.[24] In particular, use of an angle-dependent $\bar{I}_{He}$ may improve agreement of the theoretically calculated SDCS's shown in Fig. 9 with experiment for the larger angles $\theta_L$ shown.

### C. Conclusions

We have presented here in detail theoretical results for detachment of 0.5-MeV $H^-$ ions in collision with a He-atom target in which the H atom is excited to $H(2p)$ or $H(2s)$. The results are very sensitive to the detached-electron's angle of ejection in the laboratory frame. This sensitivity makes this process an ideal probe of the dynamics of the $H(n=2)$-$e^-$ three-body system for low energies in the projectile frame. In particular, laboratory-frame measurements of the DDCS's for small ejection angles may be directly related to long-range dipole interactions and shape-resonance effects in the projectile frame.

The present results for $H(n=2)$ final states, when combined with the present calculations for the DDCS's in which the H atom is left in the $H(1s)$ final state, also give greatly improved agreement with the experimental results that do not measure the final state of the H atom. This is true also for the SDCS's. Nevertheless, experimental measurements with higher angular resolutions for electron ejection in the forward direction are required to confirm in detail many of the theoretically predicted features presented here.

### ACKNOWLEDGMENTS

We gratefully acknowledge numerous stimulating conversations with Joseph H. Macek throughout the course of this work. We also thank Manuel G. Menendez and M. M. Duncan for providing us with detailed information on their experimental techniques and results. This work was supported in part by the U.S. Department of Energy, Office of Basic Energy Sciences, Division of Chemical Sciences under Grant No. DE-FG02-88ER13955.

## APPENDIX: NORMALIZATION FACTOR $N_\mu(k)$ FOR THE DIPOLE POTENTIAL

The oscillatory energy-dependent normalization factor $N_\mu(k)$ is defined as follows:[46]

$$N_\mu(k)=[B_\mu\cos^2\eta_\mu+B_\mu^{-1}(1+\mathcal{G}_\mu^2)\sin^2\eta_\mu - \mathcal{G}_\mu\sin2\eta_\mu]^{1/2} , \quad \text{(A1)}$$

where $\eta_\mu$ is the phase shift in the $\mu$th channel [cf. Eq. (18)] and where $B_\mu$ and $\mathcal{G}_\mu$ are analytic functions defined by[43]

$$B_\mu=\frac{\sinh\pi\alpha_\mu}{\cosh\pi\alpha_\mu-\cos2[\alpha_\mu\ln(k/2)+x_\mu]} , \quad \text{(A2a)}$$

$$\mathcal{G}_\mu=\frac{-\sin2[\alpha_\mu\ln(k/2)+x_\mu]}{\cosh\pi\alpha_\mu-\cos2[\alpha_\mu\ln(k/2)+x_\mu]} . \quad \text{(A2b)}$$

The parameters $\alpha_\mu$ and $x_\mu$ are defined in Eqs. (19b) and (19e).


[1]M. J. Seaton, Proc. Phys. Soc. (London) **77**, 174 (1961).

[2]M. Gailitis and R. Damburg, Proc. Phys. Soc. **82**, 192 (1963); Zh. Eksp. Teor. Fiz. **44**, 1644 (1963) [Sov. Phys.—JETP **17**, 1107 (1963)]; M. Gailitis, in *Atomic Physics 6,* edited by R. Damburg and O. Kukaine (Plenum, New York, 1978), pp. 249–266.

[3](a) J. Macek and P. G. Burke, Proc. Phys. Soc. **92**, 351 (1967); (b) J. Macek, *ibid.* **92**, 365 (1967).

[4]C. R. Liu and A. F. Starace, Phys. Rev. Lett. **62**, 407 (1989).

[5]See the papers in *Electronic and Atomic Collisions,* edited by N. Oda and K. Takayanagi (North-Holland, Amsterdam, 1980), pp. 619–672.

[6]J. S. Risley, in Ref. 5, pp. 619–633.

[7]R. L. Champion, Adv. Electron. Electron Phys. **58**, 143 (1982).

[8]J. S. Risley, Comments At. Mol. Phys. **12**, 215 (1983).

[9]M. E. Rudd and J. H. Macek, Case Stud. At. Phys. **3**, 47 (1972).

[10]F. Drepper and J. S. Briggs, J. Phys. B **9**, 2063 (1976).

[11](a) M. G. Menendez and M. M. Duncan, Phys. Rev. Lett. **40**, 1642 (1978); (b) Phys. Rev. A **20**, 2327 (1979); (c) J. H. Macek, M. G. Menendez, and M. M. Duncan, *ibid.* **29**, 516 (1984); (d) M. M. Duncan, M. G. Menendez, and J. L. Hopkins, *ibid.* **30**, 655 (1984); (e) M. M. Duncan, M. G. Menendez, J. L. Hopkins, and C. B. Mauldin, Phys. Rev. Lett. **55**, 1983 (1985); (f) M. M. Duncan, M. G. Menendez, C. B. Mauldin, and J. L. Hopkins, Phys. Rev. A **34**, 4657 (1986); (g) M. G. Menendez and M. M. Duncan, *ibid.* **36**, 1653 (1987); (h) M. M. Duncan and M. G. Menendez, Phys. Rev. A **39**, 1534 (1989).

[12]M. R. Frantz, L. A. Wright, and T. C. Genoni, Phys. Rev. A **24**, 1135 (1981).

[13]M. H. Day, Phys. Rev. A **26**, 1260 (1982).

[14]N. Maleki and J. H. Macek, Phys. Rev. A **26**, 3198 (1982).

[15]O. H. Crawford, Phys. Lett. **104A**, 25 (1984).

[16]C.-H. Park, A. F. Starace, and J. H. Macek, Phys. Rev A **31**, 1336 (1985).

[17]L. A. Wright, M. R. Franz, and T. C. Genoni, Phys. Rev. A **32**, 1215 (1985).

[18](a) L. H. Andersen, J. P. Bangsgaard, and J. Sørensen, Phys. Rev. Lett. **57**, 1558 (1986); (b) J. Sørensen, L. H. Andersen, and L. B. Nielsen, J. Phys. B **21**, 847 (1988).

[19]The Appendix of Ref. 16 contains three misprints. Also, the calculated results of Ref. 16 contain two errors. We note these in the following. (a) Equation (A3) should read, $\zeta\equiv K/2k_i+K_{\min}/K$. (b) In Eq. (A6a), the coefficient of $T_4$ should be $3(1-\zeta^2)^2/8$. (c) In Eq. (A6c) the coefficient of $T_4$ should be $-(15\zeta^4-18\zeta^2+3)/4$. (d) All doubly differential cross sections in Figs. 1–6 should be divided by 4. (e) The single differential cross sections in Fig. 7 are incorrect. See Fig. 10 of this paper for the correct results.

[20]Cf. Ref. 16, Eq. (12).

[21]Cf. Ref. 16, Sec. III A.

[22]Y. K. Kim and M. Inokuti, Phys. Rev. **165**, 39 (1968).

[23]J. H. Hubbell, W. J. Veigele, E. A. Briggs, R. T. Brown, D. T. Cromer, and R. J. Howerton, J. Phys. Chem. Ref. Data **4**, 471 (1975).

[24]Y. T. Lee and J. C. Y. Chen, Phys. Rev. A **19**, 526 (1979). Cf. Eqs. (3.10)–(3.12).

[25]J. Macek, J. Phys. B **1**, 831 (1968).

[26]U. Fano, Rep. Prog. Phys. **46**, 97 (1983).

[27]A. F. Starace, in *Fundamental Processes of Atomic Dynamics,* edited by J. S. Briggs, H. Kleinpoppen, and H. O. Lutz (Plenum, New York, 1988), pp. 235–258.

[28]C. D. Lin, Phys. Rev. Lett. **35**, 1150 (1975).

[29]C. Greene, U. Fano, and G. Strinati, Phys. Rev. A **19**, 1485 (1979). Note that we take $\theta_\mu$ in the same quadrant as $-\alpha_\mu\ln\frac{1}{2}k-x_\mu$.

[30]Cf. Eq. (30a) of Ref. 16.

[31]Cf. Eq. (30b) of Ref. 16.

[32]Cf. A. R. Edmonds, *Angular Momentum in Quantum Mechanics* 2nd ed. (Princeton University Press, Princeton, NJ, 1960), Eq. (4.6.5).

[33]A. P. Yutsis, I. B. Levinson, and V. V. Vanagas, *The Theory of Angular Momentum* (Israel Program for Scientific Translations, Jerusalem, 1962), Eq. (A.7.5).

[34](a) Cf. Ref. 33, Eq. (A.7.2); (b) cf. Ref. 33, Eq. (A.6.6).

[35]Cf. Ref. 32, Eq. (4.6.6).

[36]E. W. Hobson, *The Theory of Spherical and Ellipsoidal Harmonics* (Cambridge University Press, Cambridge, 1931), p. 360.

[37]Chang-Hwang Park, Ph.D. thesis, The University of Nebraska, 1984.

[38]Chih-Ray Liu, Ph.D. thesis, The University of Nebraska, 1988.

[39]*Handbook of Mathematical Functions,* edited by M. Abramowitz and I. A. Stegun (Dover, New York, 1965), Chap. 9.

[40]J. T. Broad and W. P. Reinhardt, Phys. Rev. A **14**, 2159 (1976).

[41]H. C. Bryant, B. D. Dieterle, J. Donahue, H. Sharifian, H. Tootoonchi, D. M. Wolfe, P. A. M. Gram, and M. A. Yates-Williams, Phys. Rev. Lett. **38**, 228 (1977); H. C. Bryant, D. A. Clark, K. B. Butterfield, C. A. Frost, H. Sharifian, H. Tootoonchi, J. B. Donahue, P. A. M. Gram, M. E. Hamm, R. W. Hamm, J. C. Pratt, M. A. Yates, and W. W. Smith, Phys. Rev. A **27**, 2889 (1983).

[42]M. G. Menendez and M. M. Duncan (private communication).
[43]U. Fano and A. R. P. Rau, *Atomic Collisions and Spectra* (Academic, New York, 1986), Secs. 5.4 and 5.7.3.
[44]J. S. Briggs and K. Taulbjerg, in *Structure and Collisions of Ions and Atoms,* Vol. 5 of *Topics of Current Physics,* edited by I. A. Sellin (Springer, Berlin, 1978), pp. 105–153.
[45]L. A. Wright, T. C. Genoni, and M. R. Franz, Bull. Am. Phys. Soc. **28**, 799 (1983).
[46]C. Greene, U. Fano, and G. Strinati, Phys. Rev. A **19**, 1485 (1979).